LANGMUIR

pubs.acs.org/Langmuir Article

Deposition of Cubic Copper Nanoparticles on Silicon Laser-Induced Periodic Surface Structures via Reactive Laser Ablation in Liquid

Eric J. Broadhead, Avery Monroe, and Katharine Moore Tibbetts*

Cite This: *Langmuir* 2021, 37, 3740−3750 Read Online

ACCESS | Metrics & More | Article Recommendations | Supporting Information

ABSTRACT: We report the deposition of cubic copper nanoparticles (Cu NPs) of varying size and particle density on silicon laser-induced periodic surface structures via reactive laser ablation in liquid (RLAL) using intense femtosecond laser pulses. Two syntheses were compared: (1) simultaneous deposition, wherein a silicon wafer was laser-processed in aqueous $Cu(NO_3)_2$ solution and (2) sequential deposition, wherein the silicon wafer was laser-processed in water and then exposed to aqueous $Cu(NO_3)_2$. Only simultaneous deposition resulted in high Cu loading and cubic Cu NPs deposited on the surface. The solution pH, $Cu(NO_3)_2$ concentration, and sample translation rate were varied to determine their effects on the size, morphology, and density of Cu NPs. Solution pH near ∼6.8 maximized Cu deposition. The $Cu(NO_3)_2$ concentration affected the Cu NP morphology but not the size or Cu loading. The sample translation rate most significantly affected the Cu loading, particle size, and particle density. The observed synthesis parameter dependence of these Cu NP properties resembles results by electrodeposition to grow Cu NPs on silicon surfaces, which suggests that Cu NP deposition by RLAL follows a mechanism similar to electrodeposition.

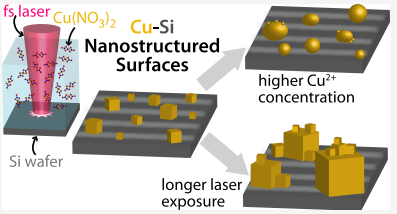

INTRODUCTION

Metallic nanoparticles are of considerable interest, as quantum size effects, high surface to volume ratios, and changes in surface plasmon resonance are all size-specific properties that can be tuned through efficient synthesis methods.[1−3] Copper is of particular importance because it is an excellent conductor of heat and electricity and much cheaper than other plasmonic metals.[4] Hence, copper nanoparticles (Cu NPs) are used in various applications, including biological sensing and imaging,[5,6] antimicrobial applications,[7] and catalysis.[8] In addition, the oxides of copper (CuO and Cu_2O) that typically form on the surfaces of Cu NPs can be useful for catalysis,[9,10] solar cells,[11] and selective biofiltering of viruses.[12] Depositing Cu NPs on silicon is particularly interesting due to the potential applications of copper silicides as high capacity hosts for lithium battery anodes.[13,14] Cu NPs are often synthesized through wet chemical methods, such as deposition−precipitation, ammonia evaporation, electrodeposition, and strong electrostatic adsorption; however, these methods can be time-consuming, involve multiple steps, and result in Cu NPs with broad size distributions or low Cu loading.[8,15−19]

Over the past decade, laser ablation in liquid has gained increasing attention as a synthesis route to metal NPs that represents a simpler, faster, and more green synthesis method compared to conventional wet chemical methods.[20] Reactive laser ablation in liquid (RLAL) in particular is rapidly emerging as a robust synthesis route to multicomponent nanomaterials.[21−23] RLAL involves focusing intense laser pulses onto a solid target such as silicon immersed in liquid, typically a solution of a metal salt. The ablation of silicon with laser pulses has been widely observed to generate laser-induced periodic surface structures (LIPSS).[24,25] The laser-silicon interaction also generates a plasma containing reactive electrons, radicals, and ions at the solid−liquid interface.[26] These highly nonequilibrium conditions can generate stable nanomaterials comprised of the target material and the metal in solution that are free of capping agents.[20] In addition, this synthesis is considered as a "green" method because these materials are generated in ambient conditions under water.[27] The metal salt used in RLAL is easily interchangeable and provides a simple synthesis method to produce to core/shell nanoparticles,[28,29] metal phyllosilicates,[30] and silver−silicon surfaces for use in SERS.[31] Recently, we have shown that RLAL can produce gold−silicon nanostructured surfaces (NSSs) with unique properties and a pH-dependent gold deposition mechanism.[32] Although RLAL has been used to synthesize various metal-NSSs, especially for use in SERS, the methods' viability with copper, a material that is typically challenging to reduce and stabilize, is a yet unexamined area of interest.

In this work, we report the formation of Cu-NSSs via RLAL. Cu-NSSs were synthesized by two different methods: (1) simultaneous deposition, in which the silicon target is ablated in aqueous $Cu(NO_3)_2$ solution, and (2) sequential deposition,

Received: January 25, 2021
Revised: March 8, 2021
Published: March 19, 2021

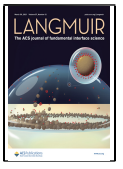

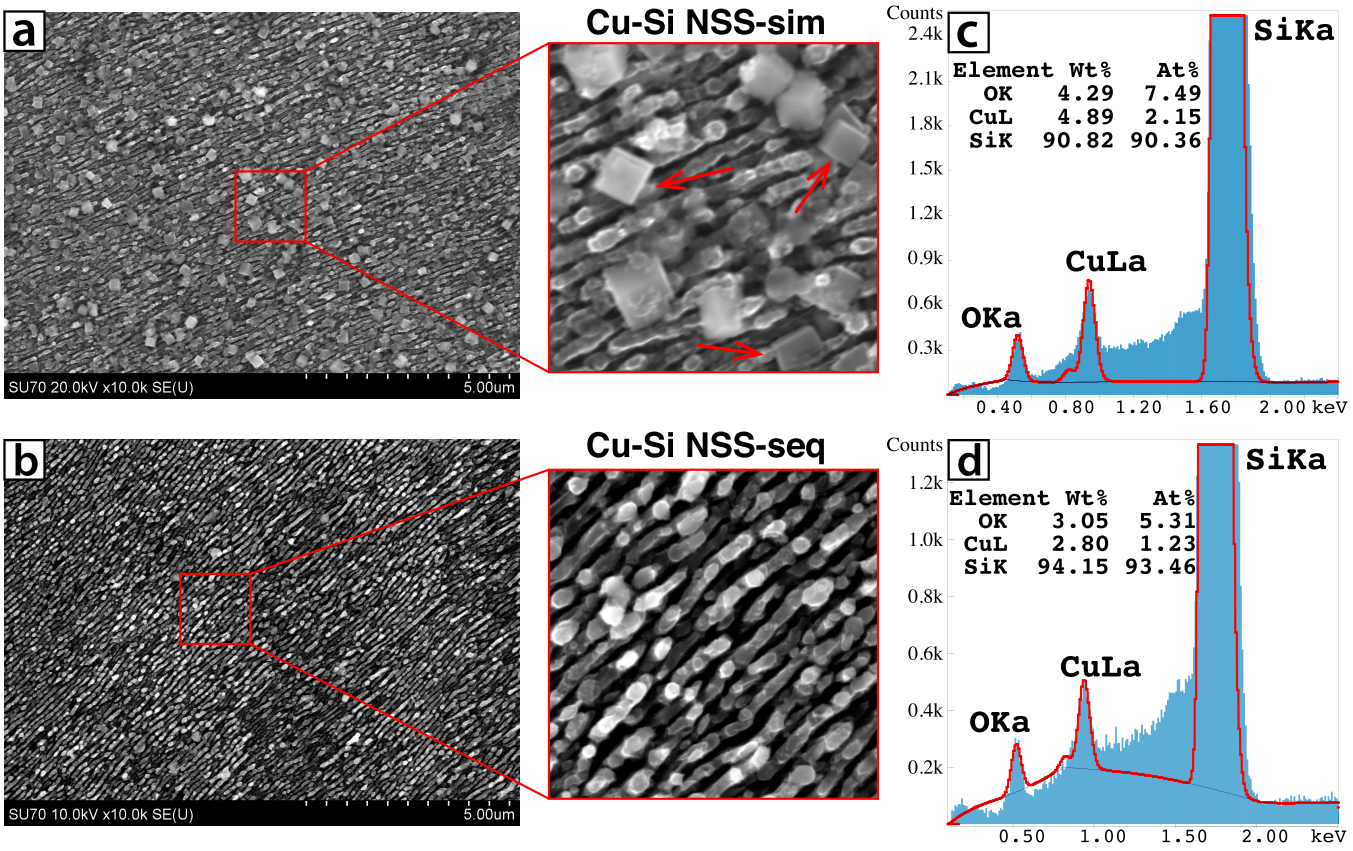

Figure 1. (a) SEM image of a silicon wafer ablated in 1.0 mM $Cu(NO_3)_2$ at pH 6.8 (Cu-Si NSS-sim), with inset depicting cubic Cu. (b) SEM image of a silicon wafer ablated in deionized water then soaked in 1.0 mM $Cu(NO_3)_2$ at pH 6.8 (Cu-Si NSS-seq), with inset depicting the lack of visible Cu NPs. Panels (c, d) show EDX spectra corresponding to (a, b), respectively.

in which the silicon target is ablated in water and the laser-processed surface subsequently exposed to aqueous $Cu(NO_3)_2$. Whereas sequential deposition resulted in low Cu-loading with the majority of Cu diffused into the silicon substrate, simultaneous deposition resulted in high Cu loading with cubic Cu NPs on the Cu-NSS when the pH of the precursor solution was fixed to ~6.8. These cubic Cu NPs were assigned to a Cu^0 core/Cu_2O shell structure on the basis of XRD and XPS analysis. Further XPS depth profiling analysis showed that Cu penetrated at least ~90 nm into the silicon wafer for both simultaneous and sequential deposition. Altering the copper precursor concentration and the sample translation rate changed the shape and size of the Cu NPs, respectively. The underlying mechanism of Cu NP deposition in RLAL can be understood in the context of copper electrodeposition onto silicon. Although the deposited Cu NPs are often larger than the typical 100 nm threshold for the term "nanoparticles", we still use this term because the chemistry of their formation is understood in the context of nanoparticle growth mechanisms. Our results provide a basis for further optimization of Cu deposition by RLAL to provide access to interfacial materials for applications in which high Cu_2O/Cu loading is needed, such as biological sensing and imaging, catalysis, solar cells, and hosts for lithium battery anodes.

EXPERIMENTAL SECTION

Materials. Silicon wafers (n-doped, (111)-oriented, single side polished, and 300 μm thick (NOVA electronic materials) were used as received. Copper(II) nitrate hemi(pentahydrate) [$Cu(NO_3)_2$, Alfa Aesar] and potassium hydroxide (KOH, Fisher Scientific) were made into stock solutions using deionized water purified by a Millipore Ultrapure water system (resistivity of 18.2 MΩ cm^{-1} at 25 °C).

Sample Preparation. Stock solutions of 25 mM $Cu(NO_3)_2$ and 100 mM KOH were prepared and used to make the working solutions. The working solutions had a $Cu(NO_3)_2$ concentration of 1.0 or 4.0 mM, and the KOH concentration was varied from 1.0 to 4.0 mM to control the solution pH. The working solutions were prepared several hours prior to synthesis and stored at 6 °C. Solution pH was measured with a SevenExcellence pH meter, standardized to buffers pH 4, 7, and 10. A 10 × 10 × 40 mm quartz fluorimeter cuvette was cleaned with aqua regia, rinsed thoroughly with water, dried and then equilibrated to room temperature. Approximately 3.0 mL of the working solution was transferred to this cuvette and a pre-cut silicon wafer was placed inside, held flat against the back of the cuvette using a small stopper so that the silicon wafer remained perpendicular to the laser.

Instrumentation. The laser processing setup has been described in detail previously in refs 23 and 32. The cuvette containing the silicon wafer and working solution was placed approximately 10 mm before the focal point of the f = 50 mm lens. The pulse energy was attenuated to 100 μJ for the ablation experiments. The laser spot size was measured to be 85 μm using a light microscope on an ablated silicon wafer. Under these conditions, the laser fluence and laser intensity were calculated to be 1.8 J cm^{-2} and 5.8 × 10^{13} W cm^{-2}, respectively (Supporting Information, Fluence & Peak Intensity Calculations). The cuvette was translated in the x- and y-directions (perpendicular to laser beam propagation) at a fixed rate of 0.05, 0.1, or 0.2 mm/s during irradiation using a motorized stage (Thorlabs) to move the laser focus across the silicon wafer. Samples were translated 6 mm horizontally and 12 mm vertically, giving a laser-processed area of 72 mm^2. A 1 kHz laser repetition rate results in approximately 500 pulses hitting each laser spot at a translation rate of 0.2 mm/s, 1000 pulses at 0.1 mm/s, and 2000 pulses at 0.05 mm/s. Following laser

https://doi.org/10.1021/acs.langmuir.1c00238
Langmuir 2021, 37, 3740−3750

processing, silicon wafers were rinsed with deionized water and ethanol then dried with nitrogen and stored for characterization.

Characterization. *Scanning Electron Microscopy Energy-Dispersive X-ray Spectroscopy (SEM–EDX).* Surface imaging and elemental analysis were conducted using a Hitachi FE SEM SU-70 (spatial resolution 1.0 nm) equipped with an energy-dispersive X-ray spectroscopy (EDX) detector. Images were obtained at 10–20 keV, and elemental analysis with mapping was conducted at 20 keV. GENESIS spectrum (EDX) software was used to display EDX spectra and conduct elemental quantification. Samples were prepared by placing the synthesized copper–silicon wafers onto a Hitachi M4 aluminum specimen mount (6 mm), held in place by a PELCO tab (12 mm OD). To improve conductivity and image resolution, a small piece of 3 M copper conductive tape (6.3 mm W × 16.46 mm L) was placed onto the sample, touching both the silicon wafer and the aluminum specimen mount.

X-ray Diffraction (XRD). XRD spectra were collected on an Empyrean Panalytical diffractometer, equipped with a 4 kW X-ray generator and a PIXcel 3D-Medipix 3 detector. Samples were run at 45 kV and 40 mA using a 3-axis chi-phi-z stage with a beam radius of 240 mm over the 2θ range of 25–75°. Samples were placed on the chi-phi-z stage, holding the wafers in place with either the provided clamps or double-sided tape. Sample placement was aligned using an internal instrumental camera and by running a z-auto align program to maximize signal.

X-ray Photoelectron Spectroscopy (XPS). XPS spectra were collected on a PHI 5000 VersaProbe III using a monochromatic Al Kα X-ray source (1486.6 eV), with a typical resolution of 0.4–0.5 eV. Samples were scanned over 1.4 mm with an X-ray beam of 200 μm. Selected samples were also examined in profile mode in which the samples were processed with an argon ion beam that etched away layers of the sample. This allowed for the removal of any potential contaminants (excess carbon or oxidation) and for examination of the changing species makeup with depth. The provided stage was cleaned with ethanol and dried to remove excess carbon. Samples were then placed and held onto the stage with double-sided tape. Spectra were processed in MultiPak XPS, with corrections applied based upon the C 1s peak shift to center at 284.8 eV.

RESULTS AND DISCUSSION

Effects of Simultaneous and Sequential Laser Processing on Cu Deposition. To determine the effect of Cu^{2+} ions in solution on the outcome of laser processing, silicon wafers were (1) processed in 1 mM $Cu(NO_3)_2$ solution and (2) processed in water and then soaked in 1 mM $Cu(NO_3)_2$ solution. Both samples were run under the same laser and sample translation conditions and with the $Cu(NO_3)_2$ solution fixed at pH 6.8. Samples first processed in water were soaked in the copper solution for approximately 45 min, the same amount of time required for laser processing in solution. Sample (1) is labeled Cu-Si NSS-sim (simultaneous) and sample (2) is labeled Cu-Si NSS-seq (sequential) in accordance with the timing of the silicon wafers' exposure to Cu^{2+} ions, either simultaneously with the laser processing, or sequentially, with copper exposure after laser processing.

Figure 1 shows SEM images of Cu-Si NSS-sim (a) and Cu-Si NSS-seq (b). The Cu-Si NSS-sim inset image shows large, cubic Cu NPs across the LIPSS of the sample surface. In contrast, the Cu-Si NSS-seq inset image shows no visible Cu NPs at all, with a surface that resembles that of Si LIPSS obtained upon processing in water (Supporting Information, Figure S1). Both surfaces have LIPSS with a period of approximately 100 nm, similar to prior work.[25,33−36] However, the large Cu NPs deposited onto the LIPSS of the Cu-Si NSS-sim sample are completely different from earlier results from our group using gold ions: small Au NPs (~10–30 nm) were distributed homogeneously across the surface of the LIPSS when the silicon wafer was processed simultaneously with $KAuCl_4$ in solution.[32] Moreover, the deposition of Ag onto silicon through electroless deposition (analogous to sequential processing) results in dendrite-like structures,[37,38] and deposition of Ag onto silicon through simultaneous laser processing produces smaller, more homogeneous Ag NPs.[31] These results suggest a distinct Cu^{2+} deposition mechanism compared to other metal ions, both with and without simultaneous laser processing.

Figure 1c shows the EDX spectrum of a Cu-Si NSS-sim sample with composition of 4.89 wt % Cu, 4.29 wt % O, and 90.82 wt % Si. The EDX spectrum of the Cu-Si NSS-seq sample (Figure 1d) indicates some Cu deposition despite the lack of clearly visible Cu NPs, with 2.80 wt % Cu, 3.05 wt % O, and 94.15 wt % Si. The 2.80 wt % Cu may be expected on the basis of prior observation of Au deposition under similar conditions,[32] but the lower Cu amount compared to the Cu-Si NSS-sim sample indicates that simultaneous processing of Si wafers in Cu^{2+} solution results in more favorable Cu deposition.

Both the simultaneous and sequential samples were characterized using EDX mapping to determine the distribution of Cu on the surfaces. Figure 2 shows representative EDX mapping results of a Cu-Si NSS-sim sample with the SEM image (top left) and mapping of Cu (top right), Si (bottom left), and O (bottom right). When comparing the SEM with the Cu EDX mapping, it is clear that the large cubic structures seen scattered across the surface have a high Cu content, as the areas with the highest density of Cu in the Cu EDX mapping strongly align with the positioning of the cubic structures in the SEM images, as indicated by the magenta circle. The cubic Cu NP circled in the top left image corresponds nearly perfectly with a spike in Cu density in the Cu mapping and a slight decrease in intensity in the Si EDX mapping. In contrast, the lack of visible Cu NPs in the Cu-Si NSS-seq sample was consistent with Cu EDX mapping results showing Cu homogeneously distributed across the surface (Supporting Information, Figure S2). This result suggests that Cu in the Cu-Si NSS-seq sample is either present as small NPs outside the range of the SEM magnification used or that it is diffused into the silicon surface.

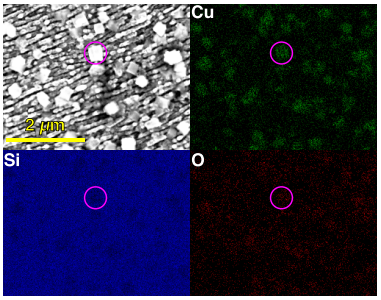

Figure 2. SEM image of a silicon wafer ablated in 1.0 mM $Cu(NO_3)_2$ fixed at pH 6.8 (top left) with subsequent mapping images (Cu top right, Si bottom left, and O bottom right). Highlighted in the pink circle is a cubic Cu NP in the SEM image, the spike in Cu intensity in the mapping images where the Cu NP lies, and the decrease in Si intensity in the Si mapping.

Figure 3 shows the XRD spectrum of the Cu-Si NSS-sim (red) and Cu-Si NSS-seq (blue) obtained over the range of approximately 25–75° to exclude a signal from amorphous

https://doi.org/10.1021/acs.langmuir.1c00238
Langmuir 2021, 37, 3740−3750

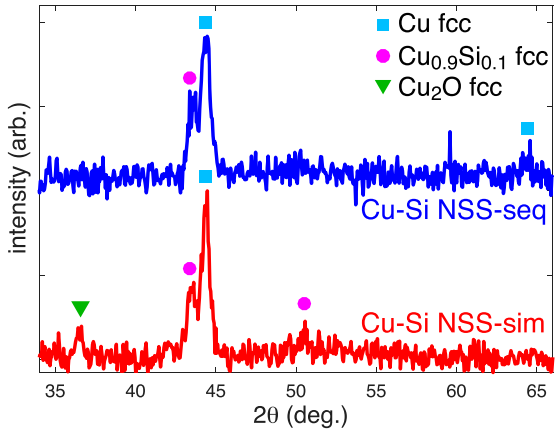

Figure 3. XRD spectra of the Cu-Si NSS-sim (red) and Cu-Si NSS-seq (blue) with JCDD references for Cu fcc, $Cu_{0.9}Si_{0.1}$ fcc, and Cu_2O indicated.

silica. Four distinct peaks were found in the Cu-Si NSS-sim spectrum, matching three JCDD references: the peak at ~36.5° matched JCDD reference 01-085-8590 for cubic cupric oxide (Cu_2O); the peaks at ~43.2 and ~50.5° matched JCDD reference 04-015-2819 for copper silicide ($Cu_{0.9}Si_{0.1}$); and the peak at ~44.2° matched JCDD reference 01-080-5762 for cubic copper metal. The Cu-Si NSS-seq spectrum was similar to the Cu-Si NSS-sim spectrum, with the peaks at ~43.2 and ~44.2° both present. However, the peak near ~36.5°, representing Cu_2O, is absent in the Cu-Si NSS-seq spectrum. This result combined with visual examination of the Cu-Si NSS-sim and Cu-Si NSS-seq images in Figure 1, suggests that the large cubic Cu NPs seen in the Cu-Si NSS-sim sample but absent in the Cu-Si NSS-seq sample likely contain Cu_2O. It is notable that copper metal and copper silicide were present on both samples.

The Cu-Si NSS-sim and Cu-Si NSS-seq were further analyzed by XPS with argon ion depth profiling (Figures 4–6). The Ar^+ energy was set to 3 kV and sputtering was conducted over a 1 × 1 mm area. With these conditions, the sample is etched at approximately 6.0 nm per minute for a

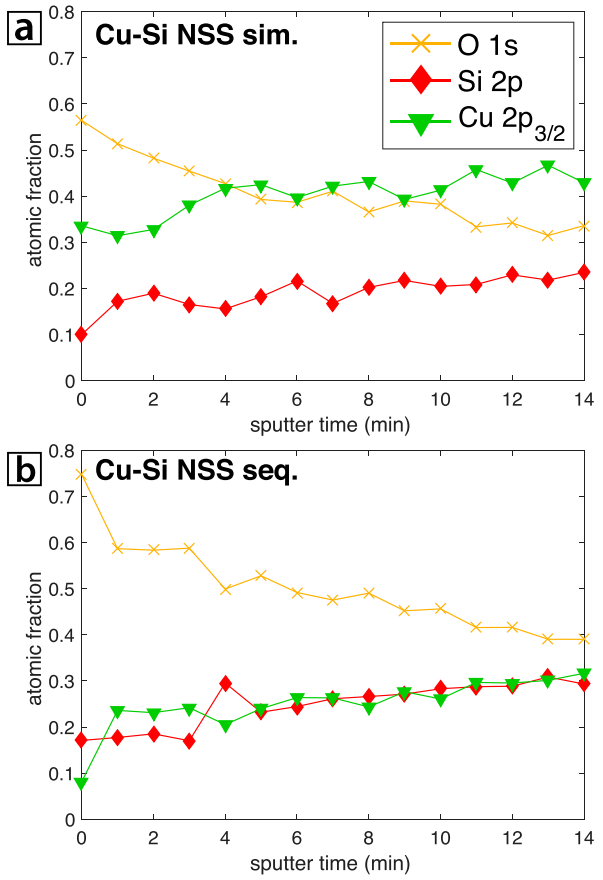

Figure 5. XPS depth profiling spectra of Cu-Si NSS-sim (a) and Cu-Si NSS-seq. (b). The atomic fraction of the species present is shown with respect to sputter time.

surface of silicon dioxide on silicon (SiO_2/Si).[39] Hence, every 3 min in sputter time represented in Figure 4 is equivalent to an approximately 18 nm increase in depth, resulting in a final depth of 90 nm after 15 min of sputter time. However, this assumption likely underestimates the depth because the SiO_x species are etched away with increased sputter time. Hence,

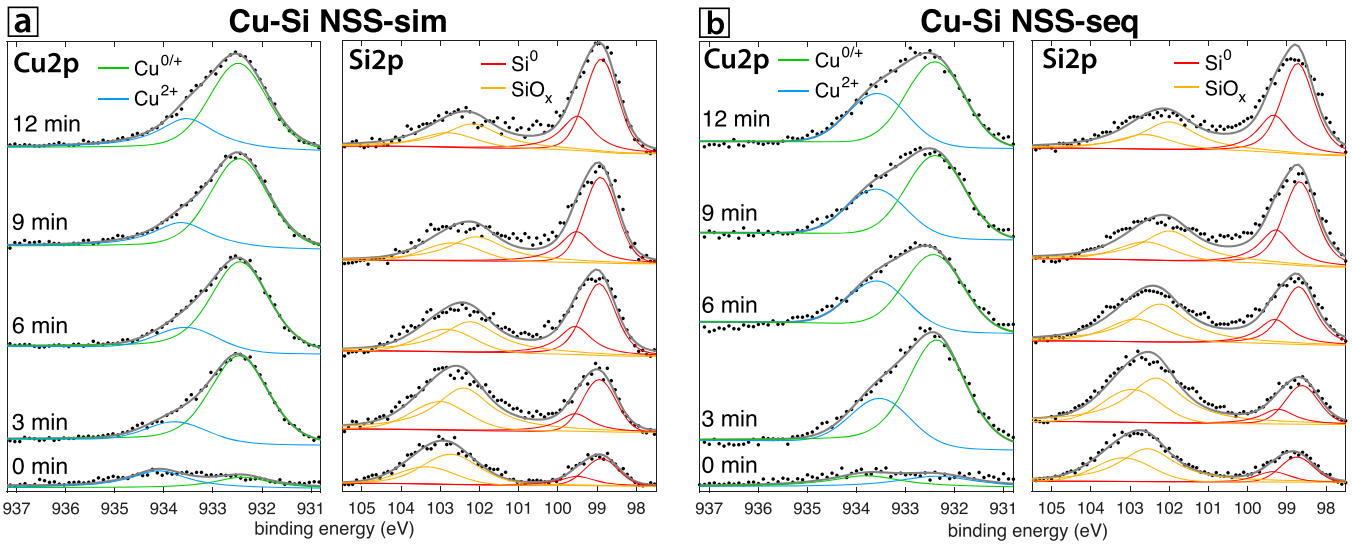

Figure 4. XPS depth profiling spectra of Cu-Si NSS-sim (a) and Cu-Si NSS-seq. (b). The change in the Cu 2p and Si 2p spectra are shown with respect to sputter time.

https://doi.org/10.1021/acs.langmuir.1c00238
Langmuir 2021, 37, 3740−3750

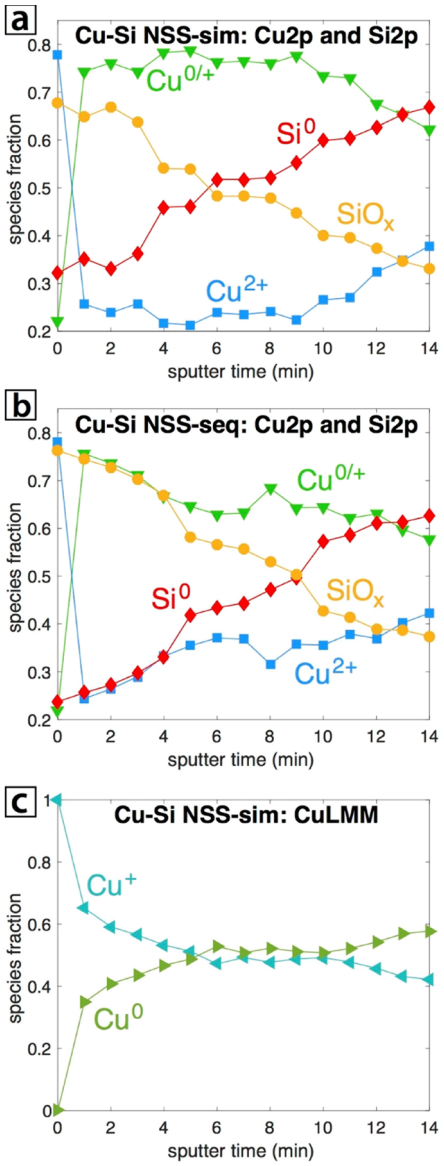

Figure 6. XPS depth profiling spectra of Cu-Si NSS-sim (a) Cu-Si NSS-seq (b). The quantified species fraction from Figure 4 are shown with respect to sputter time. (c) Cu LMM spectra of the Cu-Si NSS-sim with respect to sputter time.

the sputter rate would likely increase after the removal of the SiO_x species due to a higher etch rate of 7.8 nm per minute for silicon,[39] so a final depth of 90 nm represents a conservative lower bound.

Figure 4 shows the Cu 2p and Si 2p XPS spectra at a series of sputter times indicated on the left panels for Cu-Si NSS-sim (a) and Cu-Si NSS-seq (b). The Si^0 doublet in both samples appears downshifted from the generally accepted 99.4 eV value for the Si 2p peak.[40] This slight downshifting in the Si^0 doublet has been observed in silica colloids obtained from femtosecond laser ablation before[23,32,41] and likely indicates increased electron density around the Si atoms.[42,43] The high contribution of SiO_x species at earlier sputter times is due to oxidation of surface Si atoms by reactive water species such as hydroxyl radicals produced during ablation.[44,45] In both samples, the rapid decrease of SiO_x (orange) and increase of Si^0 doublet peaks (red) with sputter time indicate that SiO_x species are rapidly etched away. These results indicate that the Ar^+ ion sputtering penetrates into the surface over the course of sputter time, rather than just probing the "valleys" of the LIPSS structures because SiO_x would still be present on these regions due to exposure to the aqueous solution. Before sputtering, only one copper peak at ~934 eV is present in both samples, assigned to Cu^{2+} in copper(II) oxide due to the presence of satellite features (Supporting Information, Figure S3).[46] The Cu^{2+} satellite disappears within 3 min (Supporting Information Figure S3), despite the continued presence of the 934 eV peak at longer sputter times. Hence, the 934 eV feature likely contains contributions from copper silicide, which has a binding energy near that of copper oxide.[47,48] This assignment is consistent with the XRD results (Figure 3) indicating the presence of copper silicide in both the simultaneous and sequential samples. As sputter time increases, a second feature near ~933 eV is observed, corresponding to Cu^0, Cu^+, or both.[49,50] The signal of both Cu species increased with sputter time for both samples, although the simultaneous sample had a higher ratio of $Cu^{0/+}$ to Cu^{2+}. The lower amounts of $Cu^{0/+}$ in the sequential samples is likely due to the lack of both Cu_2O (Figure 3) and visible Cu NPs (Figure 1).

Figure 5a shows the atomic fraction of the O 1s, Si 2p, and Cu 2p obtained from Cu-Si NSS-sim. The oxygen content of the surface steadily decreased as sputter time increased, whereas silicon and copper increased with sputter time. The increase in the copper content with penetration depth suggests that not only does the copper form the large Cu NPs seen in Figure 1 but it also penetrates at least ~90 nm into the silicon surface on the basis of the estimated sputter etch rate constant of 6 nm/min and the 15 min of sputter time plotted in Figure 5. This extensive penetration is similar to the behavior of Au deposited under similar conditions.[32] Because a sputter area of 1 mm^2 is much larger than the Cu NPs in Cu-Si NSS-sim (Figures 1 and 2), the sputtering should average out over the areas with and without Cu NPs. The Cu-Si NSS-seq (Figure 5b) shows some similar trends to the simultaneous sample, but with some key differences. Oxygen content of the surface decreased more rapidly than that for the Cu-Si NSS-sim over the course of the depth profiling. At all depths, the Cu content of the sequential sample is lower than that for the simultaneous sample, reaching only about 75% of the fractional component at the final sputter time of 14 min (0.4 for the Cu-Si NSS-sim, 0.3 for the Cu-Si NSS-seq). This reaffirms the results in Figure 1, where Cu-Si NSS-seq had lower levels of copper deposition than those seen in Cu-Si NSS-sim. In addition, Cu-Si NSS-seq had a much lower atomic % of Cu at the surface (i.e., at 0 min of sputter time) when compared to the Cu-Si NSS-sim spectrum, providing further evidence that the majority of the Cu present in the Cu-Si NSS-seq sample is diffused into silicon. It is important to note that Cu may be overrepresented in the XPS spectra due to its drastically higher kinetic energies when compared, in part because of the use of a monochromatic X-ray source.[51]

The quantified yields of the Cu and Si species obtained from depth profiling are shown in Figure 6 for Cu-Si NSS-sim (a) and Cu-Si NSS-seq (b). Both samples show a significant increase in $Cu^{0/+}$ relative to Cu^{2+} after the initial scan at 0 min followed by a decrease of this ratio at longer sputter times. Similarly, an increase of Si^0 and decrease of SiO_x with sputter time is observed. The Cu-Si NSS-sim sample clearly has more $Cu^{0/+}$ relative to Cu^{2+} than the Cu-Si NSS-seq sample. This difference could be due to the large Cu NPs on the surface of the Cu-Si NSS-sim sample, resulting in more $Cu^{0/+}$ species

https://doi.org/10.1021/acs.langmuir.1c00238
Langmuir 2021, 37, 3740−3750

observed deeper into the sample. In both samples, copper diffusing into the surface likely reacts with silicon to form copper silicides,[52−54] which would account for the increasing Cu^{2+} content deeper into the sample.

To distinguish between Cu^0 and Cu^+, the Cu LMM spectra of a Cu-Si NSS-sim sample were examined with depth profiling (Supporting Information, Figure S4). Two features were observed: 568 eV, assigned to Cu^0 and 570 eV, assigned to Cu^+.[55] Figure 6c shows the species fraction for Cu^0 (green) and Cu^+ (blue) with respect to sputter time. The initial spectrum with pure Cu^+ (0 min) shifts to an increasing fraction of Cu^0 with respect to sputter time, until the sample is majority Cu^0 by the end (14 min).[55] These data, coupled with the imaged Cu NPs on a Cu-Si NSS-sim sample in Figure 1 and the XRD spectrum in Figure 3, provide evidence that the large cubic NPs on the Cu-Si NSS-sim samples are Cu_2O shell/Cu^0 core NPs.

Effects of Synthesis Conditions on Simultaneous Cu Deposition. Consistent with our previous work using gold,[32] both the simultaneous and sequential samples showed substantial Cu penetration into the silicon substrate, suggesting that metal penetration into silicon requires only a laser-processed surface and sufficient exposure time. Nevertheless, the data in Figures 1−6 indicate that the simultaneous method is much more efficient at depositing Cu onto the Si substrate than the sequential method. Moreover, only simultaneous deposition produces cubic NPs on the surface (Figures 1 and 2) that appear to be Cu_2O shell/Cu^0 core structures (Figures 3 and 6c). To further explore the extent to which copper deposition can be controlled in simultaneous processing, three key synthesis parameters were varied: the pH of the $Cu(NO_3)_2$ precursor solution, the concentration of $Cu(NO_3)_2$, and the sample translation rate.

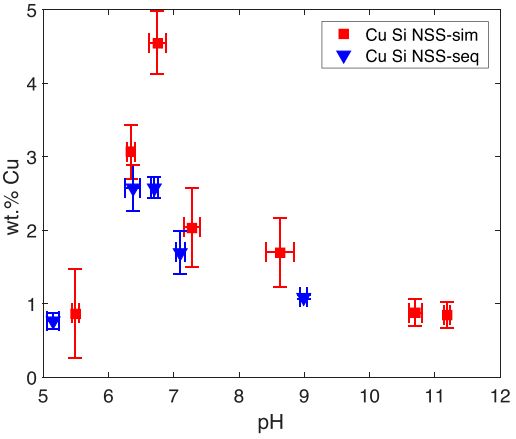

Figure 7. Copper deposition (wt %) on the Cu-Si NSS-sim and Cu-Si NSS-seq as a function of precursor solution pH.

Solution pH. The pH of the $Cu(NO_3)_2$ precursor solution was varied from 5 to 11 using different amounts of added KOH. EDX spectra for each resulting Cu-Si NSS-sim were obtained by scanning an area of approximately 62 × 62 μm. Figure 8 shows the mean Cu wt % deposition obtained by EDX as a function of the initial $Cu(NO_3)_2$ solution pH (red squares). Error bars on the ordinate and abscissa axes represent standard deviation over at least three individual samples. Solutions with a low pH (<6.0) or with a high pH (>7.0) consistently resulted in much lower copper deposition than

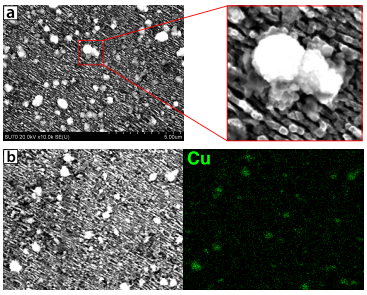

Figure 8. (a) SEM image of a silicon wafer ablated in 4.0 mM $Cu(NO_3)_2$ at pH 6.8 with an inset on the right hand side depicting Cu NPs and (b) its subsequent SEM image and Cu EDX mapping, confirming the bright spots on the SEM images as Cu NPs.

solutions in a tight neutral range (6.0−7.0), especially near pH ∼6.8. For comparison, the Cu content of the Cu-Si NSS-seq samples were also plotted against solution pH for a similar set of pH values (blue triangles) Each Cu-Si NSS-seq set had at least two individual samples. In the pH range of 5−9, the Cu-Si NSS-seq samples had modestly lower Cu wt % values compared to the Cu-Si NSS-sim samples. However, the Cu-Si NSS-sim samples run near pH 6.8 had by far the largest amount of copper deposition. On the basis of these results, the precursor solution pH for subsequent syntheses was fixed at approximately 6.8 to maximize Cu deposition on the Cu-Si NSS-sim samples.

Cu Concentration. The concentration of the $Cu(NO_3)_2$ was increased from 1.0 to 4.0 mM to determine how the Cu^{2+} concentration affected Cu deposition. A 4.0 mM concentration was chosen because it was assumed sufficiently high to potentially increase the Cu content, but not high enough to cause extensive precursor absorption at the 800 nm laser wavelength, which would inhibit surface ablation. Figure 8a shows an SEM image of a silicon wafer ablated in 4.0 mM $Cu(NO_3)_2$ at pH 6.8 with an inset further highlighting a Cu NP. The Cu NPs that formed on these samples tended to have a more amorphous, almost spherical shape compared with the cubic NPs from the 1.0 mM samples (Figure 1). Figure 8b shows an SEM image with its Cu EDX mapping to its right. Once again, bright spots on the SEM image are confirmed to be Cu NPs, as their positions align with areas of increased Cu density in the EDX mapping image. The EDX spectrum (Supporting Information, Figure S5) shows the sample contained 4.92 Cu wt %, similar to the Cu-Si NSS-sim samples with a concentration of 1.0 mM $Cu(NO_3)_2$ at pH 6.8. The XRD spectrum of the 4.0 mM sample (Supporting Information, Figure S6) has identical peaks to that of the 1.0 mM sample (Figure 3). It is notable that although increasing the concentration of the precursor solution did not significantly increase the copper content, it altered the morphology of the Cu NPs deposited on the silicon surface. This finding will be further discussed in the discussion section with regards to the electrodeposition mechanisms that govern this morphology change.

Sample Translation Rate. The scanning speed of the motorized stage used for sample translation was varied to examine the effect of deposition time on the Cu-Si NSSs. For the samples shown in Figures 1−8, the translation rate was 0.2 mm/s (12 mm/min), corresponding to approximately 500 pulses per spot (Experimental Section, Instrumentation). Studies were carried out on samples using translation rates of 0.1 mm/s (6 mm/min, 1000 pulses per spot) and 0.05 mm/

https://doi.org/10.1021/acs.langmuir.1c00238
Langmuir 2021, 37, 3740−3750

s (3 mm/min, 2000 pulses per spot), motivated by the observation that increasing exposure time in the electrodeposition technique resulted in an increase in Cu deposition on a Si surface but not a change in NP shape.[56] Figure 9a

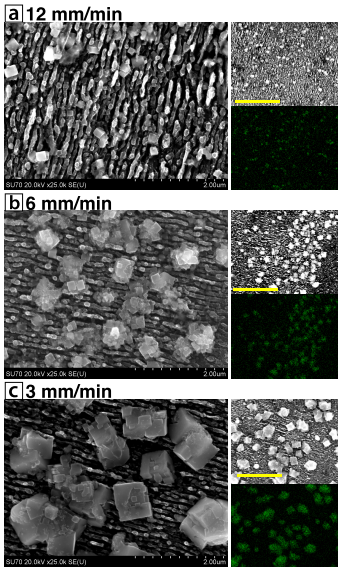

Figure 9. SEM images of silicon wafers ablated in 1.0 mM $Cu(NO_3)_2$ at pH 6.8 with insets to the right depicting an SEM image at ×10.0 k magnification with Cu EDX mapping (scale bars are 5 μm). Sample translation rate is (a) 12, (b) 6, and (c) 3 mm/min.

shows an SEM image (left) with Cu EDX mapping (right) of a sample ablated with a scanning speed of 12 mm/min, similar to the Cu-Si NSS-sim sample shown in Figures 1 and 2. Cu NPs on these surfaces are isolated cubes that are sporadically dispersed across the surface of the silicon wafer. When the translation rate is halved to 6 mm/min (Figure 9b), the Cu NPs still appear to be cubic in shape and appear at a similar density, but the particles are slightly larger, and it appears that some particles consist of multiple cubic Cu NPs coalesced together. The EDX spectrum of this sample (Supporting Information, Figure S7) indicates ~6.1 Cu wt %, slightly higher than the ~4.9 wt % obtained at 12 mm/min. The XRD spectrum (Figure S8) indicates the same Cu_2O, Cu, and $Cu_{0.9}Si_{0.1}$ species previously seen in Figure 3. At 3 mm/min (Figure 9c) a dramatic shift in morphology is observed: Cu NPs appear at a lower density but a greatly increased size and often consist of multiple smaller cubic Cu NPs coalesced with larger NPs. The EDX spectrum of this sample (Figure S9) indicates ~11.7 Cu wt %, substantially higher than the other samples. The XRD spectrum (Figure S10) has the same three species as the prior samples. Interestingly, while increasing the concentration of the precursor solution changed the shape of the NPs but not the Cu content on the Si surface, changing the translation rate did not change the NP shapes but did affect the Cu content, especially when slowing to 3 mm/min. A similar phenomenon was seen when Cu NPs were deposited by electrodeposition.[56]

Table 1 summarizes the effects of changing the precursor concentration and translation rate on the NP shape, Cu wt %, NP density, and NP size. Average NP density and size were obtained using ImageJ by counting all visible nanoparticles seen in SEM images at ×10.0 k magnification (a range of ~161 μm^2). Holding the concentration constant at 1.0 mM and slowing the translation rate substantially increased the Cu content from 4.6, to 6.1, to 11.7 wt %. Lowering the translation rate from 12 to 6 mm/min caused a small increase in NP size but no significant change in NP density. The most significant effects were seen decreasing further to a scanning speed of 3 mm/min, with NP density decreasing from 0.63 to 0.27 NPs/μm^2, and NP size nearly doubling. Comparing the samples in which the precursor concentration was varied but scanning speed was held constant (1.0 mM vs 4.0 mM at 12 mm/min) shows that the Cu content was unchanged, with a moderate decrease in density and no significant change in size.

Copper Deposition Mechanisms. The dependence of the Cu content in the Cu-Si NSS on the solution pH can be rationalized by the expected pH-dependent reduction rate of the $Cu(NO_3)_2$ complex and its interactions with ablated silicon species. The laser reduction of copper nitrate is primarily driven by hydrated electrons in solution, which form both from water photolysis and ejection from the silicon surface.[57−59] However, hydrated electrons are rapidly scavenged under acidic conditions,[60,61] which is expected to slow Cu^{2+} reduction. Slow Cu^{2+} reduction is consistent with the extremely low deposition of copper onto silica ejected from the silicon surface during RLAL under acidic conditions.[41] In contrast, high copper loading on ejected silica species observed in RLAL under basic conditions is consistent with faster reduction. Moreover, the formation of silicic acid in solution at pH >8[30] results in further conversion of Cu^{2+} into copper phyllosilicates with strong Cu−O−Si bonds.[41] This consumption of copper in solution reactions to form phyllosilicates at high pH likely inhibits copper deposition onto the Si surface, resulting in the observed low Cu loadings on the Cu-Si NSS at high pH (Figure 7). Hence, a neutral solution pH results in optimal deposition because the Cu^{2+} can be reduced at a sufficient rate, but no silicic acid is formed, mitigating the incorporation of Cu^{2+} into phyllosilicates. This trend is consistent with our earlier work where the deposition of gold onto silicon required a neutral pH to enable efficient deposition of Au NPs onto the silicon surface.[32] In the case of gold, basic solution pH inhibited deposition because most $[AuCl_4]^-$ was reduced too quickly by hydrated electrons in solution.

Varying both the sample translation rate and precursor concentration resulted in similar effects on the deposited Cu NP morphologies and loading as observed by electrodeposition.[56] Electrodeposition is a well-established method that produces metallic coatings on a substrate by passing an

Table 1. Effects of Concentration and Translation Rate on NP Shape, Cu wt %, Density, and Size

$Cu(NO_3)_2$ concentration	translation rate	NP shape	Cu wt %	NPs/μm^2	NP size (μm)
1.0 mM	12 mm/min	cubic	4.6	0.65 ± 0.13	0.17 ± 0.07
1.0 mM	6 mm/min	cubic	6.1	0.62 ± 0.12	0.22 ± 0.05
1.0 mM	3 mm/min	cubic	11.7	0.27 ± 0.10	0.39 ± 0.09
4.0 mM	12 mm/min	amorphous	4.9	0.46 ± 0.19	0.18 ± 0.06

https://doi.org/10.1021/acs.langmuir.1c00238
Langmuir 2021, 37, 3740−3750

electric current through a solution containing metal salt.[62] The copper ions in solution (typically from copper sulfate or copper nitrate) are reduced from Cu^{2+} to Cu^0 by the electric current. These Cu^0 atoms then can nucleate and grow in Cu clusters and NPs.[63] The morphology and Cu loading can be tuned in electrodeposition based upon a number of factors, most notably the Cu^{2+} concentration and deposition time.[56,63] Increasing the Cu^{2+} concentration results in a change in the NP shape from cubic to octahedral, whereas longer deposition time increases Cu loading.[56] The similar trends observed in this work with RLAL and previous electrodeposition studies can be rationalized by analogous deposition mechanisms: hydrated electrons produced by the laser pulses act as the reducing agent, as does the electric current in electrodeposition.

In any deposition method forming metal NPs on supports, the particle morphology, size distribution, and number density are affected by two key processes: nucleation and diffusion-limited growth.[56,64,65] Depending upon the metal and support chosen, nucleation can be progressive or instantaneous. The nucleation of copper on silicon crystals (both n- and p-type) is well known to be progressive, meaning that new nucleation sites will be continuously created as deposition time goes on.[64] The growth, however, can follow three different methods: the Frank-van der Merwe method (layer-by-layer), the Volmer−Weber method (island), or the Stranski−Krastanov method (mixed layer and island).[66] Cu NPs follow the Volmer−Weber growth mode, driven by the weak interaction between Cu and Si. This "island" mechanism results in increasing particle size with increasing deposition time in electrodeposition.[64,66] Our result that increased deposition time resulted in larger particle sizes and is also consistent with the Volmer−Weber mechanism because decreased sample translation rate exposes the surface to more laser pulses, which generates more electrons for Cu^{2+} reduction. The final shape of the Cu NP deposited on the Si support is ultimately determined by the surface planes with slower growth rates, which are the (100) and (111) planes for Cu.[64] Depending upon the growth rates of these planes, different facets will be exposed on the NP, controlling its shape. At low Cu precursor concentrations, the growth rate of the (111) planes are faster than the growth rates of the (100) planes, resulting in the exposure of (100) facets to form cubic Cu NPs,[56] as the face-centered cubic crystal has six (100) facets exposed. Conversely, when the precursor concentration is increased, the growth rate of the (100) planes equalizes to the (111) planes, resulting in mixed facet exposure. This circumstance will alter the Cu NP shape to form a truncated octahedron or cuboctahedron.[56] Our results that the higher Cu precursor concentration resulted in Cu NPs with more spherical morphology further confirms that RLAL emulates electrodeposition: mixed facet exposure occurs at high precursor concentrations, altering the shape of the Cu NPs. Interestingly, in electrodeposition, the cubic NPs seen at the "low" concentration occurred at 5−10 mM, and the cuboctahedron shapes seen at the "high" concentration began to appear near 50 mM, suggesting that RLAL may be reducing the Cu precursor much more efficiently, thereby altering the NP shapes at lower precursor concentrations.[56] This increased localized deposition efficiency can be rationalized by the extremely high electron density in laser-induced plasmas at the water−silicon interface.[67]

For any growth mechanism, the size of the Cu NPs is dependent upon the supersaturation factor; the ratio of the pressure experienced by the optimum-sized NP to that of a growing particle at a particular size, concentration, and temperature.[66] Essentially, a NP will continue to grow given enough time to do so, until it reaches the optimum size, at which point the particle growth will stop. In electrodeposition, increasing the deposition time will increase the amount of charge transfer, in turning causing the particle size to increase and the pressure to decrease. This process will continue until the supersaturation factor gets closer to 1, reaching the optimum size.[56] As deposition of Cu onto Si is based upon a progressive nucleation of metal clusters and subsequent island growth on the support,[66] new nucleation sites are continuously created as the Cu NPs continue to grow at previously formed sites. The NPs that formed at the first nucleation sites will reach the optimum size first and stop growing.[56] However, when most particles reach the optimum size and deposition still continues, particles can begin to coalesce, which was seen at the slowest sample translation rate (Figure 9c). One potential explanation for this NP coalescence is Ostwald ripening in which small particles can coalesce onto larger particles.[68] Larger particles are much more thermodynamically favorable, and thus, small particles can spontaneously coalesce onto large particles in an effort to reduce their surface energy, as interior atoms are bonded to more neighbors and will be more stable.[69] Another potential explanation for the formation of the large cubic Cu NPs lies in the nature of femtosecond laser ablation. At a sample translation rate of 3 mm/min, each 85 μm spot will be hit by ∼2000 laser pulses. Simulations and experiments on femtosecond laser ablation have shown that the initial plasma temperature can reach 4000−5000 K,[70] temperatures at the surface will stay above the melting threshold of silicon (1685 K) and copper (1358 K) for up to 1 ns after the laser pulse is over,[71] and the plasma is completely quenched in ∼5 ns.[72] Given these high transient temperatures, it is possible that each subsequent laser pulse at a given spot can briefly disrupt the crystal lattice of the cubic Cu NPs, generating new nucleation sites. This secondary nucleation can account for the observed structures in Figure 9c consisting of small cubic NPs on top of larger cubic NPs. Hence, when deposition time in RLAL is increased by decreasing the sample translation rate, the Cu NPs have longer time to grow and more opportunity for secondary nucleation to occur. These processes result in significantly larger particles, higher Cu loading, lower particle density, and particles consisting of multiple cubic NPs coalesced together.

CONCLUSIONS

In this work, Cu-Si NSSs were produced by RLAL processing of silicon wafers immersed in $Cu(NO_3)_2$ solutions. Processing the silicon wafers sequentially resulted in low Cu-loading and no visible NPs on the surface, whereas simultaneous processing resulted in high Cu-loading when the pH was fixed to near ∼6.8. Under both conditions, copper penetrated into the silicon wafer at least ∼90 nm. Cubic Cu NPs were produced only with the simultaneous method, with XRD and XPS analysis demonstrating that they were likely Cu_2O shell/Cu^0 core NPs. Varying the precursor concentration in the simultaneous method resulted in a change in the Cu NP shape, whereas altering the deposition time resulted in a change in the NP size and Cu loading. Collectively, these results for RLAL synthesis of Cu NPs on silicon emulate results obtained by electrodeposition, suggesting the operation of similar Cu nucleation and growth mechanisms for RLAL

https://doi.org/10.1021/acs.langmuir.1c00238
Langmuir 2021, 37, 3740−3750

and electrodeposition. The utilization of these insights could allow for more efficient laser processing synthesis of copper nanomaterials for various applications.

■ ASSOCIATED CONTENT

Supporting Information

The Supporting Information is available free of charge at https://pubs.acs.org/doi/10.1021/acs.langmuir.1c00238.

Fluence and peak intensity calculations, additional SEM images, EDX spectra, XRD spectra, and XPS spectra (PDF)

■ AUTHOR INFORMATION

Corresponding Author

Katharine Moore Tibbetts − *Department of Chemistry, Virginia Commonwealth University, Richmond, Virginia 23284, United States;* orcid.org/0000-0001-8853-5656; Email: kmtibbetts@vcu.edu

Authors

Eric J. Broadhead − *Department of Chemistry, Virginia Commonwealth University, Richmond, Virginia 23284, United States*

Avery Monroe − *Department of Chemistry, Virginia Commonwealth University, Richmond, Virginia 23284, United States*

Complete contact information is available at: https://pubs.acs.org/10.1021/acs.langmuir.1c00238

Notes

The authors declare no competing financial interest.

■ ACKNOWLEDGMENTS

This work was supported by the American Chemical Society Petroleum Research Fund (57799-DNI10). A.M. was supported by an NSF-REU fellowship. We would like to acknowledge the Nanomaterials Core Characterization Facility at Virginia Commonwealth University for characterization.

■ REFERENCES

(1) Li, K.; Li, X.; Stockman, M. I.; Bergman, D. J. Surface Plasmon Amplification by Stimulated Emission in Nanolenses. *Phys. Rev. B* **2005**, *71*, 115409.

(2) Yao, J.; Liu, Z.; Liu, Y.; Wang, Y.; Sun, C.; Bartal, G.; Stacy, A. M.; Zhang, X. Optical Negative Refraction in Bulk Metamaterials of Nanowires. *Science* **2008**, *321*, 930.

(3) Eccles, J. W. L.; Bangert, U.; Bromfield, M.; Christian, P.; Harvey, A. J.; Thomas, P. UV-Vis Plasmon Studies of Metal Nanoparticles. *J. Phys.: Conf. Ser.* **2010**, *241*, No. 012090.

(4) Ikari, S.; Kashiwade, H.; Matsuoka, T.; Hirayama, T.; Ishida, S.; Kato, K. Improvement of Copper Plating Adhesion of PPE Printed Wiring Board by Plasma Treatment. *Surf. Coat. Technol.* **2008**, *202*, 5583−5585.

(5) Li, C.; Su, Y.; Zhang, S.; Lv, X.; Xia, H.; Wang, Y. An Improved Sensitivity Nonenzymatic Glucose Biosensor Based on a CuxO Modified Electrode. *Biosens. Bioelectron.* **2010**, *26*, 903−907.

(6) Liu, J.; Xue, D. Rapid and Scalable Route to CuS Biosensors: A Microwave-Assisted Cu-Complex Transformation into CuS Nanotubes for Ultrasensitive Nonenzymatic Glucose Sensor. *J. Mater. Chem.* **2011**, *21*, 223−228.

(7) Raspolli Galletti, A. M.; Antonetti, C.; Marracci, M.; Piccinelli, F.; Tellini, B. Novel Microwave-Synthesis of Cu Nanoparticles in the Absence of Any Stabilizing Agent and Their Antibacterial and Antistatic Applications. *Appl. Surf. Sci.* **2013**, *280*, 610−618.

(8) Gawande, M. B.; Goswami, A.; Felpin, F.-X.; Asefa, T.; Huang, X.; Silva, R.; Zou, X.; Zboril, R.; Varma, R. S. Cu and Cu-Based Nanoparticles: Synthesis and Applications in Catalysis. *Chem. Rev.* **2016**, *116*, 3722−3811.

(9) de Jongh, P. E.; Vanmaekelbergh, D.; Kelly, J. J. Cu2O: A Catalyst for the Photochemical Decomposition of Water? *Chem. Commun.* **1999**, 1069−1070.

(10) Grosse, P.; Yoon, A.; Rettenmaier, C.; Chee, S. W.; Cuenya, B. R. Growth Dynamics and Processes Governing the Stability of Electrodeposited Size-Controlled Cubic Cu Catalysts. *J. Phys. Chem. C* **2020**, *124*, 26908−26915.

(11) Akimoto, K.; Ishizuka, S.; Yanagita, M.; Nawa, Y.; Paul, G. K.; Sakurai, T. Thin Film Deposition of Cu2O and Application for Solar Cells. *Solar Energy* **2006**, *80*, 715−722.

(12) Borkow, G.; Sidwell, R. W.; Smee, D. F.; Barnard, D. L.; Morrey, J. D.; Lara-Villegas, H. H.; Shemer-Avni, Y.; Gabbay, J. Neutralizing Viruses in Suspensions by Copper Oxide-Based Filters. *Antimicrob. Agents Chemother.* **2007**, *51*, 2605−2607.

(13) Stokes, K.; Geaney, H.; Sheehan, M.; Borsa, D.; Ryan, K. M. Copper Silicide Nanowires as Hosts for Amorphous Si Deposition as a Route to Produce High Capacity Lithium-Ion Battery Anodes. *Nano Lett.* **2019**, *19*, 8829−8835.

(14) Aminu, I. S.; Geaney, H.; Imtiaz, S.; Adegoke, T. E.; Kapuria, N.; Collins, G. A.; Ryan, K. M. A Copper Silicide Nanofoam Current Collector for Directly Grown Si Nanowire Networks and Their Application as Lithium-Ion Anodes. *Adv. Funct. Mater.* **2020**, *30*, 2003278.

(15) Chen, L.-F.; Guo, P.-J.; Qiao, M.-H.; Yan, S.-R.; Li, H.-X.; Shen, W.; Xu, H.-L.; Fan, K.-N. Cu/SiO2 Catalysts Prepared by the Ammonia-Evaporation Method: Texture, Structure, and Catalytic Performance in Hydrogenation of Dimethyl Oxalate to Ethylene Glycol. *J. Catal.* **2008**, *257*, 172−180.

(16) Zhang, J.; Wu, D. Aqueous Phase Catalytic Hydrogenation of Furfural to Furfuryl Alcohol over In-Situ Synthesized Cu−Zn/SiO2 Catalysts. *Mater. Chem. Phys.* **2021**, *260*, 124152.

(17) Eskandari, S.; Tate, G.; Leaphart, N. R.; Regalbuto, J. R. Nanoparticle Synthesis via Electrostatic Adsorption Using Incipient Wetness Impregnation. *ACS Catal.* **2018**, *8*, 10383−10391.

(18) Xu, C.; Chen, G.; Zhao, Y.; Liu, P.; Duan, X.; Gu, L.; Fu, G.; Yuan, Y.; Zheng, N. Interfacing with Silica Boosts the Catalysis of Copper. *Nat. Commun.* **2018**, *9*, 3367.

(19) Jiao, L.; Regalbuto, J. R. The Synthesis of Highly Dispersed Noble and Base Metals on Silica via Strong Electrostatic Adsorption: I. Amorphous Silica. *J. Catal.* **2008**, *260*, 329−341.

(20) Zhang, D.; Gökce, B.; Barcikowski, S. Laser Synthesis and Processing of Colloids: Fundamentals and Applications. *Chem. Rev.* **2017**, *117*, 3990−4103.

(21) Jiménez, E.; Abderrafi, K.; Martínez-Pastor, J.; Abargues, R.; Luís Valdés, J.; Ibáñez, R. A Novel Method of Nanocrystal Fabrication Based on Laser Ablation in Liquid Environment. *Superlattices Microstruct.* **2008**, *43*, 487−493.

(22) Ermakov, V. A.; Jimenez-Villar, E.; da Silva Filho, J. M. C.; Yassitepe, E.; Mogili, N. V. V.; Iikawa, F.; de Sá, G. F.; Cesar, C. L.; Marques, F. C. Size Control of Silver-Core/Silica-Shell Nanoparticles Fabricated by Laser-Ablation-Assisted Chemical Reduction. *Langmuir* **2017**, *33*, 2257−2262.

(23) John, M. G.; Tibbetts, K. M. One-Step Femtosecond Laser Ablation Synthesis of Sub-3 Nm Gold Nanoparticles Stabilized by Silica. *Appl. Surf. Sci.* **2019**, *475*, 1048−1057.

(24) Das, S. K.; Messaoudi, H.; Debroy, A.; McGlynn, E.; Grunwald, R. Multiphoton Excitation of Surface Plasmon-Polaritons and Scaling of Nanoripple Formation in Large Bandgap Materials. *Opt. Mater. Express* **2013**, *3*, 1705−1715.

(25) Derrien, T. J.-Y.; Koter, R.; Krüger, J.; Höhm, S.; Rosenfeld, A.; Bonse, J. Plasmonic Formation Mechanism of Periodic 100-Nm-Structures upon Femtosecond Laser Irradiation of Silicon in Water. *J. Appl. Phys.* **2014**, *116*, No. 074902.

(26) Rethfeld, B.; Ivanov, D. S.; Garcia, M. E.; Anisimov, S. I. Modelling Ultrafast Laser Ablation. *J. Phys. D: Appl. Phys.* **2017**, *50*, 193001.
(27) Gökce, B.; Amendola, V.; Barcikowski, S. Opportunities and Challenges for Laser Synthesis of Colloids. *ChemPhysChem* **2017**, *18*, 983−985.
(28) Liu, P.; Chen, H.; Wang, H.; Yan, J.; Lin, Z.; Yang, G. Fabrication of Si/Au Core/Shell Nanoplasmonic Structures with Ultrasensitive Surface-Enhanced Raman Scattering for Monolayer Molecule Detection. *J. Phys. Chem. C* **2015**, *119*, 1234−1246.
(29) Jiménez, E.; Abderrafi, K.; Abargues, R.; Valdés, J. L.; Martínez-Pastor, J. P. Laser-Ablation-Induced Synthesis of SiO_2-Capped Noble Metal Nanoparticles in a Single Step. *Langmuir* **2010**, *26*, 7458−7463.
(30) John, M. G.; Tibbetts, K. M. Mechanism of Nickel Phyllosilicate Formation by Laser Ablation in Liquid. *J. Phys. Chem. C* **2020**, *124*, 13273.
(31) Lin, C.-H.; Jiang, L.; Chai, Y.-H.; Xiao, H.; Chen, S.-J.; Tsai, H.-L. One-Step Fabrication of Nanostructures by Femtosecond Laser for Surface-Enhanced Raman Scattering. *Opt. Express* **2009**, *17*, 21581−21589.
(32) Broadhead, E. J.; Tibbetts, K. M. Fabrication of Gold−Silicon Nanostructured Surfaces with Reactive Laser Ablation in Liquid. *Langmuir* **2020**, *36*, 10120−10129.
(33) Birnbaum, M. Semiconductor Surface Damage Produced by Ruby Lasers. *J. Appl. Phys.* **1965**, *36*, 3688−3689.
(34) Vorobyev, A. Y.; Guo, C. Effects of Nanostructure-Covered Femtosecond Laser-Induced Periodic Surface Structures on Optical Absorptance of Metals. *Appl. Phys. A* **2007**, *86*, 321−324.
(35) Shen, M.; Carey, J. E.; Crouch, C. H.; Kandyla, M.; Stone, H. A.; Mazur, E. High-Density Regular Arrays of Nanometer-Scale Rods Formed on Silicon Surfaces via Femtosecond Laser Irradiation in Water. *Nano Lett.* **2008**, *8*, 2087−2091.
(36) Bonse, J.; Sturm, H.; Schmidt, D.; Kautek, W. Chemical, Morphological and Accumulation Phenomena in Ultrashort-Pulse Laser Ablation of TiN in Air. *Appl. Phys. A: Mater. Sci. Process.* **2000**, *71*, 657−665.
(37) Brejna, P. R.; Griffiths, P. R. Electroless Deposition of Silver onto Silicon as a Method of Preparation of Reproducible Surface-Enhanced Raman Spectroscopy Substrates and Tip-Enhanced Raman Spectroscopy Tips. *Appl. Spectrosc.* **2010**, *64*, 493−499.
(38) Dao, T. C.; Luong, T. Q. N.; Cao, T. A.; Kieu, N. M.; Le, V. V. Application of Silver Nanodendrites Deposited on Silicon in SERS Technique for the Trace Analysis of Paraquat. *Adv. Nat. Sci: Nanosci. Nanotechnol.* **2016**, *7*, No. 015007.
(39) Calculation of Sputter Etch Rates, Technical Document TD012. VG Scientific.
(40) Aarnink, W. A. M.; Weishaupt, A.; van Silfhout, A. Angle-Resolved X-Ray Photoelectron Spectroscopy (ARXPS) and a Modified Levenberg-Marquardt Fit Procedure: A New Combination for Modeling Thin Layers. *Appl. Surf. Sci.* **1990**, *45*, 37−48.
(41) John, M. G.; Tibbetts, K. M. Controlling the Morphology of Copper-Silica Nanocomposites from Laser Ablation in Liquid. *Appl. Surf. Sci.* **2020**, *510*, 145037.
(42) Joong Kim, K.; Park, K. T.; Lee, J. W. Thickness Measurement of SiO2 Films Thinner than 1 Nm by X-Ray Photoelectron Spectroscopy. *Thin Solid Films* **2006**, *500*, 356−359.
(43) Sublemontier, O.; Nicolas, C.; Aureau, D.; Patanen, M.; Kintz, H.; Liu, X.; Gaveau, M.-A.; Le Garrec, J.-L.; Robert, E.; Barreda, F.-A.; Etcheberry, A.; Reynaud, C.; Mitchell, J. B.; Miron, C. X-Ray Photoelectron Spectroscopy of Isolated Nanoparticles. *J. Phys. Chem. Lett.* **2014**, *5*, 3399−3403.
(44) Meader, V. K.; John, M. G.; Rodrigues, C. J.; Tibbetts, K. M. Roles of Free Electrons and H_2 O_2 in the Optical Breakdown-Induced Photochemical Reduction of Aqueous $[AuCl_4]^-$. *J. Phys. Chem. A* **2017**, *121*, 6742−6754.
(45) Chin, S. L.; Lagacé, S. Generation of H_2, O_2, and H_2O_2 from Water by the Use of Intense Femtosecond Laser Pulses and the Possibility of Laser Sterilization. *Appl. Opt.* **1996**, *35*, 907−911.
(46) Tahir, D.; Tougaard, S. Electronic and Optical Properties of Cu, CuO and Cu2O Studied by Electron Spectroscopy. *J. Phys.: Condens. Matter* **2012**, *24*, 175002.
(47) Geaney, H.; Dickinson, C.; O'Dwyer, C.; Mullane, E.; Singh, A.; Ryan, K. M. Growth of Crystalline Copper Silicide Nanowires in High Yield within a High Boiling Point Solvent System. *Chem. Mater.* **2012**, *24*, 4319−4325.
(48) Bomben, K. D.; Chastain, J.; Moulder, J.; Sobol, P.; Stickle, W. *Handbook of X-Ray Photoelectron Spectroscopy*; Perken-Elmer Corporation, Physical Electronics Edition: Eden Prairie, MN, 1992; pp. 86−87.
(49) Yano, T.; Ebizuka, M.; Shibata, S.; Yamane, M. Anomalous Chemical Shifts of Cu 2p and Cu LMM Auger Spectra of Silicate Glasses. *J. Electron Spectrosc. Relat. Phenom.* **2003**, *131-132*, 133−144.
(50) Biesinger, M. C. Advanced Analysis of Copper X-Ray Photoelectron Spectra. *Surf. Interface Anal.* **2017**, *49*, 1325−1334.
(51) Bare, S. R.; Knop-Gericke, A.; Teschner, D.; Hävacker, M.; Blume, R.; Rocha, T.; Schlögl, R.; Chan, A. S. Y.; Blackwell, N.; Charochak, M. E.; ter Veen, R.; Brongersma, H. H. Surface Analysis of Zeolites: An XPS, Variable Kinetic Energy XPS, and Low Energy Ion Scattering Study. *Surf. Sci.* **2016**, *648*, 376−382.
(52) Nürnberger, P.; Reinhardt, H. M.; Rhinow, D.; Riedel, R.; Werner, S.; Hampp, N. A. Controlled Growth of Periodically Aligned Copper-silicide Nanocrystal Arrays on Silicon Directed by Laser-Induced Periodic Surface Structures (LIPSS). *Appl. Surf. Sci.* **2017**, *420*, 70−76.
(53) Scudiero, L.; Fasasi, A.; Griffiths, P. R. Characterization of a Controlled Electroless Deposition of Copper Thin Film on Germanium and Silicon Surfaces. *Appl. Surf. Sci.* **2011**, *257*, 4422−4427.
(54) Chang, C.-A. Formation of Copper Silicides from Cu(100)/Si(100) and Cu(111)/Si(111) Structures. *J. Appl. Phys.* **1990**, *67*, 566−569.
(55) Aria, A. I.; Kidambi, P. R.; Weatherup, R. S.; Xiao, L.; Williams, J. A.; Hofmann, S. Time Evolution of the Wettability of Supported Graphene under Ambient Air Exposure. *J. Phys. Chem. C* **2016**, *120*, 2215−2224.
(56) Radi, A.; Pradhan, D.; Sohn, Y.; Leung, K. T. Nanoscale Shape and Size Control of Cubic, Cuboctahedral, and Octahedral Cu−Cu_2 O Core−Shell Nanoparticles on Si(100) by One-Step, Templateless, Capping-Agent-Free Electrodeposition. *ACS Nano* **2010**, *4*, 1553−1560.
(57) Moore Tibbetts, K.; Tangeysh, B.; Odhner, J. H.; Levis, R. J. Elucidating Strong Field Photochemical Reduction Mechanisms of Aqueous [AuCl4]−: Kinetics of Multiphoton Photolysis and Radical-Mediated Reduction. *J. Phys. Chem. A* **2016**, *120*, 3562−3569.
(58) Nikogosyan, D. N.; Oraevsky, A. A.; Rupasov, V. I. Two-Photon Ionization and Dissociation of Liquid Water by Powerful Laser UV Radiation. *Chem. Phys.* **1983**, *77*, 131−143.
(59) Pommeret, S.; Gobert, F.; Mostafavi, M.; Lampre, I.; Mialocq, J.-C. Femtochemistry of the Hydrated Electron at Decimolar Concentration. *J. Phys. Chem. A* **2001**, *105*, 11400−11406.
(60) Frias Batista, L. M.; Meader, V. K.; Romero, K.; Kunzler, K.; Kabir, F.; Bullock, A.; Tibbetts, K. M. Kinetic Control of [AuCl4]− Photochemical Reduction and Gold Nanoparticle Size with Hydroxyl Radical Scavengers. *J. Phys. Chem. B* **2019**, *123*, 7204−7213.
(61) Kurihara, K.; Kizling, J.; Stenius, P.; Fendler, J. H. Laser and Pulse Radiolytically Induced Colloidal Gold Formation in Water and in Water-in-Oil Microemulsions. *J. Am. Chem. Soc.* **1983**, *105*, 2574−2579.
(62) Basile, F.; Benito, P.; Fornasari, G.; Monti, M.; Scavetta, E.; Tonelli, D.; Vaccari, A. A Novel Electrochemical Route for the Catalytic Coating of Metallic Supports. *Stud. Surf. Sci. Catal.* **2010**, *175*, 51−58.
(63) Grujicic, D.; Pesic, B. Electrodeposition of Copper: The Nucleation Mechanisms. *Electrochim. Acta* **2002**, *47*, 2901−2912.
(64) Oskam, G.; Long, J. G.; Natarajan, A.; Searson, P. C. Electrochemical Deposition of Metals onto Silicon. *J. Phys. D: Appl. Phys.* **1998**, *31*, 1927−1949.

https://doi.org/10.1021/acs.langmuir.1c00238
Langmuir 2021, 37, 3740−3750

(65) Henry, C. R. Morphology of Supported Nanoparticles. *Prog. Surf. Sci.* **2005**, *80*, 92−116.
(66) Ji, C.; Oskam, G.; Searson, P. C. Electrochemical Nucleation and Growth of Copper on Si(111). *Surf. Sci.* **2001**, *492*, 115−124.
(67) von der Linde, D.; Sokolowski-Tinten, K.; Bialkowski, J. Laser−Solid Interaction in the Femtosecond Time Regime. *Appl. Surf. Sci.* **1997**, *109-110*, 1−10.
(68) Schmelzer, J. W. P.; Abyzov, A. S. How Do Crystals Nucleate and Grow: Ostwald's Rule of Stages and Beyond. In *Thermal Physics and Thermal Analysis: From Macro to Micro, Highlighting Thermodynamics, Kinetics and Nanomaterials*; Šesták, J.; Hubík, P.; Mareš, J. J., Eds.; Hot Topics in Thermal Analysis and Calorimetry; Springer International Publishing: Cham, 2017; pp. 195−211, DOI: 10.1007/978-3-319-45899-1_9.
(69) Zhang, Z.; Wang, Z.; He, S.; Wang, C.; Jin, M.; Yin, Y. Redox Reaction Induced Ostwald Ripening for Size- and Shape-Focusing of Palladium Nanocrystals. *Chem. Sci.* **2015**, *6*, 5197−5203.
(70) Arakelyan, S.; Zhirnova, S.; Galkin, A.; Kochuev, D.; Shamanskaya, E.; Khorkov, K. The Temperature Characteristics of Plasma Induced by Femtosecond Laser Radiation. *EPJ Web Conf.* **2019**, *220*, No. 03034.
(71) Garcia-Lechuga, M.; Puerto, D.; Fuentes-Edfuf, Y.; Solis, J.; Siegel, J. Ultrafast Moving-Spot Microscopy: Birth and Growth of Laser-Induced Periodic Surface Structures. *ACS Photonics* **2016**, *3*, 1961−1967.
(72) Saraeva, I. N.; Kudryashov, S. I.; Lednev, V. N.; Makarov, S. V.; Pershin, S. M.; Rudenko, A. A.; Zayarny, D. A.; Ionin, A. A. Single- and Multishot Femtosecond Laser Ablation of Silicon and Silver in Air and Liquid Environments: Plume Dynamics and Surface Modification. *Appl. Surf. Sci.* **2019**, *476*, 576−586.

https://doi.org/10.1021/acs.langmuir.1c00238
Langmuir 2021, 37, 3740−3750